AIAA JOURNAL
Vol. 35, No. 8, August 1997

# Adaptive Finite Volume Upwind Approaches for Aeroacoustic Computations

C. J. Hwang* and J. Y. Kuo†
*National Cheng Kung University, Tainan, Taiwan 70101, Republic of China*

**The solution-adaptive cell-vertex finite volume upwind approaches on quadrilateral-triangular meshes are presented to solve the unsteady Euler equations. For the present approaches, Runge–Kutta time-integration method, Roe's Riemann solver, a modified area-averaged approach, the MUSCL differencing with two kinds of characteristic interpolation variables, and an improved solution-adaptive technique, where a new mesh-enrichment indicator for acoustic wave is developed, are included. To evaluate the present approaches, Ringleb's flow, transonic flow around the NACA 0012 airfoil, shock propagation in a channel, traveling vortex in a freestream, and an acoustic pulse in a freestream are investigated. In the comparisons of present numerical results with related exact and/or other numerical solutions, it is shown that the upwind approach with the second kind of characteristic variables is accurate and efficient, and the present adaptive technique with appropriate mesh-enrichment indicators enhances this upwind approach to capture the shock wave, vortex, and acoustic wave. By using this solution-adaptive approach to solve the vortex–shock interaction and transonic blade–vortex interaction problems, the flow phenomena and aeroacoustic behaviors are simulated.**

## Introduction

In recent years, many numerical schemes on structured meshes have been presented to solve the Euler equations for studying aeroacoustic problems.[1–4] Meadows et al.[1] used a second-order upwind finite volume method to investigate vortex–shock interaction. Although the results were encouraging, they suggested further work, such as development of higher-order accurate methods, improved boundary condition, and grid adaptation, to enhance the approach. Casper and Meadows[2] introduced the essentially nonoscillatory (ENO) schemes with a nonlinear stencil biasing to study the axisymmetric shock–vortex interaction. From the obtained results, the nonlinear biasing of stencils made ENO schemes more robust in the study of aeroacoustic problems that involved shocks. After the comparison of several higher resolution Euler schemes for aeroacoustic calculations,[3] Lin and Chin[4] used the modified finite volume methods of Osher and Chakravarthy[3] to investigate transonic vortex–blade interaction. Two dominant sound waves, transonic and compressibility waves, and three unsteady shock wave motions were simulated. For the aforementioned works, the grids were fixed. To minimize numerical dissipation and accurately resolve the aeroacoustic behaviors, grid adaptation is useful. In the computations of high-speed impulsive noise, a near-field unstructured-grid Euler solver was combined with a newly developed Kirchhoff integral method by Strawn et al.[5] This near-field Euler solver utilized a solution-adaptive grid scheme to increase the resolution of the acoustic signal. Even though the aforementioned progress for aeroacoustic computations has been achieved, it is still worthwhile to create solution-adaptive approaches, especially the development of higher-order schemes on unstructured meshes and adaptive techniques including mesh adaption, interpolation algorithm, and mesh-enrichment indicators.

Although upwind schemes automatically provide a sufficient amount of dissipation to generate stable solutions, sometimes the excessive dissipation will be harmful for aeroacoustic calculations. To reduce the numerical dissipation or improve resolution, several numerical approaches, such as those given in Refs. 6 and 7, have been presented. To match the finite difference stencil to flow physics, a rotated upwind algorithm was developed on structured rectangular grids.[6] Even though the rotated scheme can improve the resolution of numerical solution, Dadone and Grossman[6] mentioned that their formulation required the solution of two Riemann problems at each cell face. By using characteristic variables,[6] Hwang and Wu[7] modified and extended the procedure of Whitaker et al.[8] to quadrilateral-triangular meshes, where the quadrilaterals were directionally stretched in the flow regions having one-dimensional features. According to the aforementioned discussion, the creation of an accurate upwind algorithm, where the numerical formulation is simple and the numerical dissipation can be reduced, is valuable and necessary in the computations of aeroacoustic problems.

In this paper, the solution-adaptive cell-vertex finite volume upwind approaches, which include Runge–Kutta time-integration method, Roe's Riemann solver, MUSCL differencing with two kinds of characteristic variables, a modified area-averaged approach, and an improved solution-adaptive technique, are developed on quadrilateral-triangular meshes. First, Ringleb's flow, transonic flow around the NACA 0012 airfoil, shock propagation in a channel, traveling vortex in a freestream, and an acoustic pulse in a freestream are computed to evaluate the present solution-adaptive approaches. Then two aeroacoustic problems, vortex–shock interaction (VSI) and transonic blade–vortex interaction (BVI), are investigated.

## Governing Equations

By choosing the characteristic length and flow properties at the inlet or freestream conditions as reference variables, the two-dimensional Euler equations in the Cartesian coordinate system can be written in the following nondimensional form:

$$\frac{\partial U}{\partial t} + \frac{\partial E}{\partial x} + \frac{\partial G}{\partial y} = 0 \tag{1}$$

where

$$U = \begin{bmatrix} \rho \\ \rho u \\ \rho v \\ e \end{bmatrix}, \quad E = \begin{bmatrix} \rho u \\ \rho u^2 + P \\ \rho uv \\ (e + P)u \end{bmatrix}, \quad G = \begin{bmatrix} \rho v \\ \rho uv \\ \rho v^2 + P \\ (e + P)v \end{bmatrix} \tag{2}$$

The unknown variables $\rho$, $u$, $v$, and $e$ represent the gas density, velocity components in the $x$ and $y$ directions, and total energy per unit volume. Air is the working fluid and is assumed to be perfect. The pressure $P$ is defined by

$$P = (\gamma - 1)[e - (\rho/2)(u^2 + v^2)] \tag{3}$$

where the ratio of specific heat $\gamma$ is typically taken as being 1.4.

Received Oct. 18, 1996; revision received March 20, 1997; accepted for publication April 23, 1997. 

*Professor, Institute of Aeronautics and Astronautics. Member AIAA.
†Graduate Student, Institute of Aeronautics and Astronautics.

## Numerical Algorithm

By integrating Eq. (1) over space and applying Gauss' theorem, the following integral form is obtained:

$$\frac{\partial}{\partial t}\iint_{\Omega} U\,\mathrm{d}A + \int_{\partial\Omega} (E\boldsymbol{i} + G\boldsymbol{j}) \cdot \boldsymbol{n}\,\mathrm{d}\ell = 0 \tag{4}$$

where $\boldsymbol{n}$ is the outward unit normal vector. The variable $\Omega$ is the domain of computation, and $\partial\Omega$ is the boundary of the domain. By dividing the two-dimensional domain $\Omega$ into triangles/quadrilaterals and connecting the centroid of each polygon (triangle or quadrilateral) to the midpoints of its sides, the polygon is broken into subelements. As shown in Fig. 1a, a dual mesh cell $C_i$ is formed by the collection of subelements sharing the same vertex $V_i$, and the boundary of the cell is denoted by $\partial C_i$. Assuming that the flow variables at the vertex $V_i$ have average values of the integrated variables in $C_i$, Eq. (4) can be written as

$$\frac{\partial}{\partial t}(UA)_{C_i} = -\int_{\partial C_i} F(\boldsymbol{n})\,\mathrm{d}\ell \tag{5}$$

where $A$ is the area of the cell $C_i$ and $F(\boldsymbol{n})$ is the flux oriented along the outward unit normal $\boldsymbol{n}$, i.e., $F(\boldsymbol{n}) = (n_x E + n_y G)$. To achieve the time integration on the left-hand side of Eq. (5), a two-step Runge–Kutta method[9] that results in second-order time-accurate solutions is employed for unsteady flows. A four-stage Runge–Kutta scheme with nonstandard weighting of the Runge–Kutta stages, local time steps, and residual smoothing[8] is introduced to study the steady flow problems.

In the current cell-vertex formulation, the right-hand side of Eq. (5) is evaluated by

$$\int_{\partial C_i} F(\boldsymbol{n})\,\mathrm{d}\ell = \sum_{j=L(V_i)} F_{i,j}\,\Delta\ell_{i,j} \tag{6}$$

where $L(V_i)$ is the list of vertices surrounding $V_i$ and the subscript $j$ denotes the vertices contained in $L(V_i)$; $F_{i,j}$ represents the numerical approximation for the oriented flux across the dual cell edge having the boundary length $\Delta\ell_{i,j}$. In Ref. 7, the terms $\boldsymbol{n}$ and $\Delta\ell_{i,j}$ of Eq. (6) were obtained by using the area-averaged approach.[8] Thus, $\Delta mno$ is neglected, and $\Delta\ell_{i,j}$ is the length of $\overline{no}$ (see Fig. 1b). As shown in Fig. 1b, $m$ is the midpoint of side $\overline{V_iV_j}$ and $n$ and $o$ are the centroids of $\square V_iV_jV_pV_q$ and $\Delta V_iV_rV_j$, respectively. When the area of $\Delta mno$ is not negligible, the aforementioned computational domain for the time integration and dual cell edge for the flux calculations are not consistent with each other, especially for the unsteady flow calculations. Considering the computing cost and compensating for this drawback, a modified area-averaged approach is utilized. When the area of $\Delta mno$ is less than $\frac{1}{1000}$ of the area of polygon $V_iV_rV_jV_pV_q$, the original area-averaged method[8] is applied. Otherwise, the oriented fluxes across edge $\overline{nm}$ and $\overline{mo}$ are multiplied with the corresponding length of $\overline{nm}$ and $\overline{mo}$ and then added together to represent $F_{i,j}\Delta\ell_{i,j}$.

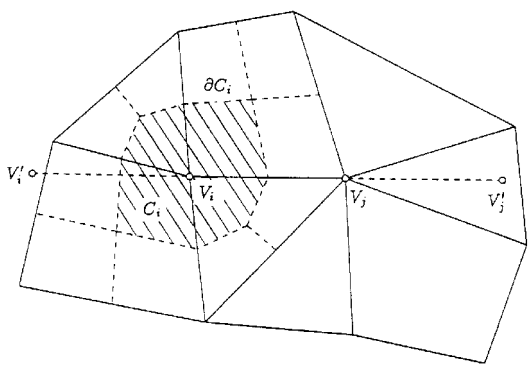


**a) Unstructured grid, dual cell, and locations of ghost nodes**

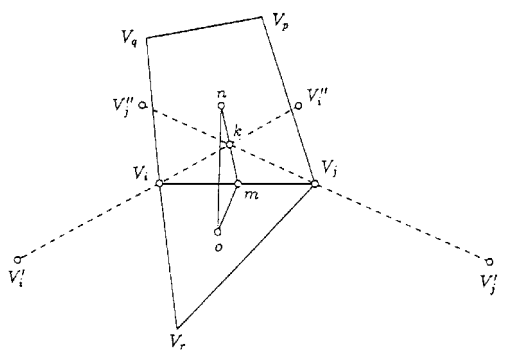


**b) Vertices, dual cell edge, and locations of ghost nodes for flux calculations**

**Fig. 1 Representative drawings.**

To formulate the upwind scheme, Roe's flux difference splitting[10] is employed. The flux at the cell interface $F_{i,j}$ can be expressed as a function of two fluid dynamic states ($U^L$ and $U^R$):

$$F_{i,j} = \tfrac{1}{2}\left[F_L + F_R - |A|(U^R - U^L)\right] \tag{7}$$

where $|A|$ is a positive definite matrix formed from the flux Jacobian $\partial F/\partial U$ (Ref. 10) and the superscripts $R$ and $L$ indicate the right and left fluid states, respectively. In this work, MUSCL differencing[11] is utilized to interpolate the properties at the cell interface using the variables at the cell vertices and ghost nodes. If the original area-averaged approach is used, the ghost nodes $V_i'$ and $V_j'$ (see Fig. 1a), which are located equidistantly along the line connecting $V_i$ and $V_j$, are introduced.[7] Otherwise, setting $V_i'V_i = V_iV_i'' = 2V_ik$ (see Fig. 1b), the ghost nodes $V_i'$ and $V_i''$ are located along the line connecting $k$ (the midpoint of edge $\overline{nm}$) and $V_i$. Similarly, the ghost nodes $V_j'$ and $V_j''$ with $V_j'V_j = V_jV_j'' = 2V_jk$ are allocated along the line connecting $k$ and $V_j$. To evaluate the state variables at ghost nodes, a simple interpolation technique[7,8] is adopted.

The quantity $U$ appearing in Eq. (7) is the vector of conserved variables as given in Eq. (1). An alternate selection is to use the primitive variables

$$V = (\rho \quad u \quad v \quad P)^T \tag{8}$$

The use of characteristic variables is another sophisticated choice. In this paper, two kinds of characteristic variables are used. The first one, whose propagation directions are set to be normal and tangential to a cell edge, was presented by Dadone and Grossman.[6] The other one is obtained based on the concept of Hirsch decomposition.[12] The vector of characteristic variables is expressed as

$$W = \begin{bmatrix} \dfrac{P + \rho_k a_k(\kappa_{2x}u + \kappa_{2y}v)}{2a_k^2} \\ \dfrac{P - \rho_k a_k(\kappa_{2x}u + \kappa_{2y}v)}{2a_k^2} \\ \rho_k(-\kappa_{1y}u + \kappa_{1x}v) \\ \rho - \dfrac{P}{a_k^2} \end{bmatrix} \tag{9}$$

where the subscript $k$ refers to the position at which the wave slopes are evaluated. The transformation matrix between $V$ and $W$ is given by

$$R = \begin{bmatrix} 1 & 1 & 0 & 1 \\ \dfrac{a_k\kappa_{1x}}{\rho_k H} & -\dfrac{a_k\kappa_{1x}}{\rho_k H} & -\dfrac{\kappa_{2y}}{\rho_k H} & 0 \\ \dfrac{a_k\kappa_{1y}}{\rho_k H} & -\dfrac{a_k\kappa_{1y}}{\rho_k H} & \dfrac{\kappa_{2x}}{\rho_k H} & 0 \\ a_k^2 & a_k^2 & 0 & 0 \end{bmatrix} \tag{10}$$

where $H = \kappa_1 \cdot \kappa_2$. Referring to Levy et al.[13] and Powell and van Leer,[14] $\kappa_1 = (\kappa_{1x}, \kappa_{1y}) = (\cos\theta_1, \sin\theta_1)$ is the direction for the velocity-component convection, and it is related to the direction of pressure gradients and velocity; $\kappa_2 = (\kappa_{2x}, \kappa_{2y}) = (\cos\theta_2, \sin\theta_2)$ is the direction for the acousticlike convection, and it is related to the strain-rate tensor. In this work, the mathematical expressions of

$\theta_1$ and $\theta_2$, which were given in Refs. 13 and 14, respectively, are adopted.

To prevent numerical oscillations near the high gradient regions, the minimum–modulus (MINMOD) limiter function[11] is employed. By combining the characteristic variables with the limiter function, the MUSCL differencing formulas can be written as

$$V^L = V_i + \tfrac{1}{4} R_i[(1 - \kappa)\bar{\Delta}_- + (1 + \kappa)\bar{\Delta}_+]W_i \tag{11a}$$

$$V^R = V_j - \tfrac{1}{4} R_j[(1 - \kappa)\bar{\Delta}_+ + (1 + \kappa)\bar{\Delta}_-]W_j \tag{11b}$$

where $R$ is the transformation matrix between primitive and characteristic variables. The definitions of $\bar{\Delta}_-$ and $\bar{\Delta}_+$ are given as follows:

$$\bar{\Delta}_- W = \text{minmod}(\Delta_- W, \beta\Delta_+ W) \tag{12a}$$

$$\bar{\Delta}_+ W = \text{minmod}(\Delta_+ W, \beta\Delta_- W) \tag{12b}$$

where minmod indicates the symbol of MINMOD function[7] and the backward and forward differences are, respectively, $\Delta_- W_i = W_i - W_{i-1}$, $\Delta_+ W_i = W_{i+1} - W_i$, $\Delta_- W_j = W_j - W_{j-1}$, and $\Delta_+ W_j = W_{j+1} - W_j$. The parameter $\kappa$, which controls the spatial accuracy, is taken as being $\frac{1}{3}$, and the compression factor $\beta$ is no greater than $(3 - \kappa)/(1 - \kappa)$.

## Boundary Conditions

At the wall, the free-slip condition is specified. For the transonic flow around the NACA 0012, the rotated extrapolation technique[7] is adopted. In the computations of shock propagation, VSI and BVI problems, the pressure is estimated by using $x$- and $y$-momentum equations

$$\rho(y_\eta u - x_\eta v)(y_\xi u_\xi - x_\xi v_\xi) = (x_\xi^2 + y_\xi^2) P_\eta - (x_\xi x_\eta + y_\xi y_\eta) P_\xi \tag{13}$$

where $\xi$ and $\eta$ represent the body-fitted coordinate lines. At an inlet, outlet, or far-field boundary, the specified condition or one-dimensional characteristic analysis based on Riemann invariants is used. For the BVI problem, one-dimensional unsteady nonreflective boundary conditions[15] are employed.

## Solution-Adaptive Technique

A solution-adaptive technique on quadrilateral-triangular meshes, which consists of the mesh generation method, mesh-enrichment indicator, two-level refinement procedure, and minimum norm network interpolation algorithm, was proposed by Hwang and Fang.[16] Referring to the background mesh, which was fixed during the unsteady calculations, all added nodes on the refined mesh were labeled. Then the properties on those labeled nodes were obtained by the interpolation from those on the background mesh. It is obvious that the accuracy of unsteady solutions was affected by the numerical interpolation. To reduce the number of interpolations, the nodes on the refined mesh, which do not appear on the background mesh but exist on the last adapted mesh, are not labeled. In other words, only those nodes that do not appear on both of the background and last adapted meshes are identified as the added nodes, and their corresponding properties are obtained by the interpolation from those on the background mesh.

To accurately and efficiently capture the acoustic signal, a new mesh-enrichment indicator is developed in this work. From the continuity equation, the dilatation is denoted as

$$\Delta = \nabla \cdot \boldsymbol{V} = -\frac{1}{\rho}\frac{\mathrm{D}\rho}{\mathrm{D}t} \tag{14}$$

and it is equal to zero at the peak or valley of acoustic wave. Therefore, any one cell, where the dilatations at the corresponding nodes have the positive and negative values, is possible to be labeled for refinement. To reduce unwanted cell refinement due to the small numerical fluctuations, the magnitude of dilatation gradient cannot be too small. Also, based on the radiation properties of acoustic waves, the projective value of dilatation gradient on the direction of wave propagation is not small. Considering the decay of acoustic signal, mesh size, and preceding discussion, any cell that satisfies the following Eqs. (15) will be labeled. In the present work, $C_1$ and $C_2$ are chosen to be 0.4:

$$A|\nabla\Delta| > C_1(A|\nabla\Delta|)_{\text{avg}} \tag{15a}$$

$$|\nabla\Delta \cdot \boldsymbol{\alpha}| > C_2 \tag{15b}$$

respectively. $A$ is the area of cell, and $\boldsymbol{\alpha}$ is the corresponding position vector referred to the reference point of the sound source. For the labeled cell, both the cell and its surrounding cells will be enriched simultaneously. If the acoustic source is not a vortex, such as the acoustic pulse in a freestream, it is not necessary to specify the location of acoustic source. In other words, Eq. (15b) is not adopted in these kinds of problems. For the VSI and BVI cases, the vortex center is chosen as the reference point of the sound source. In the present calculations, the approximate location of vortex center ($X_v = X_0 + U_\infty t$, $Y_v = Y_0$) is specified. If the location of vortex center is not specified, i.e., Eq. (15b) is not used, the acoustic signals still can be captured, but the unwanted cell refinement around the vortex is observed. Besides the density gradient[16] and dilatation, the vorticity is adopted as the mesh-enrichment indicator, so that the behaviors of traveling vortex and vortex-related interactions in aeroacoustic problems can be correctly predicted.

## Results and Discussion

### Evaluation of the Present Approaches

*Ringleb's Flow*

To evaluate the accuracy of present approaches, the problem of Ringleb's flow is studied. The analytical solution of Ringleb's flow[17] is used as a compared exact solution. As shown in Fig. 2a, four kinds of meshes are used. The $L_2$ norm of error is defined as

$$L_2 = \left[\frac{\sum_{i=1}^{N}(Q_e - Q_{ni})^2}{N}\right]^{\frac{1}{2}} \tag{16}$$

where $N$ is the total node number of the mesh. $Q_e$ and $Q_n$ represent the exact and numerical solutions, respectively. In this test, all boundary nodes are set to be exact values and not included in the $L_2$ calculation. Both the method presented by Hwang and Wu[7] and the present approaches using the modified area-averaged treatment and MUSCL differencing with the first kind of characteristic variables[6] (approach I) or with the second kind of characteristic variables (approach II) are examined. By choosing $\Delta L$ as the average value of the node spacing, Fig. 2b shows the $L_2$ norm of the density error on these four kinds of meshes. It is apparent that the modified area-averaged treatment can reduce the numerical error, and using the second kind of characteristic variables is suggested. By performing the power regression analysis on four data groups using the curves $y = ax + b$, where $a$ is equivalent to the order of the solution in $\Delta x$ and $\Delta y$, Table 1 lists the data fitting of the results shown in Fig. 2b. Among all, approach II provides the lowest absolute error norm and the highest order of accuracy.

*Transonic Flow Around the NACA 0012 Airfoil*

To further evaluate the present upwind approaches, a NACA 0012 airfoil transonic flow with a Mach number of 0.8 and the angle of attack equal to 1.25 deg is investigated. In this study, the outer boundary is taken as a rectangle of 21 × 20 chords. On a quadrilateral-triangular mesh system (see Fig. 10 in Ref. 7; 9644 elements, 6241 nodes), the aforementioned three methods are utilized again. The pressure coefficient distributions along the airfoil surface and the convergence histories are plotted in Figs. 3a and 3b, respectively. From the results shown in Fig. 3a, it is apparent that the present two approaches produce the higher resolution around the weak shock

**Table 1 Data fitting of Fig. 2b by curve $y = ax + b$**

| Method | $a$ | $b$ |
|---|---|---|
| Hwang and Wu[7] | 1.773 | −1.021 |
| Approach I | 2.745 | −0.532 |
| Approach II | 2.838 | −0.611 |

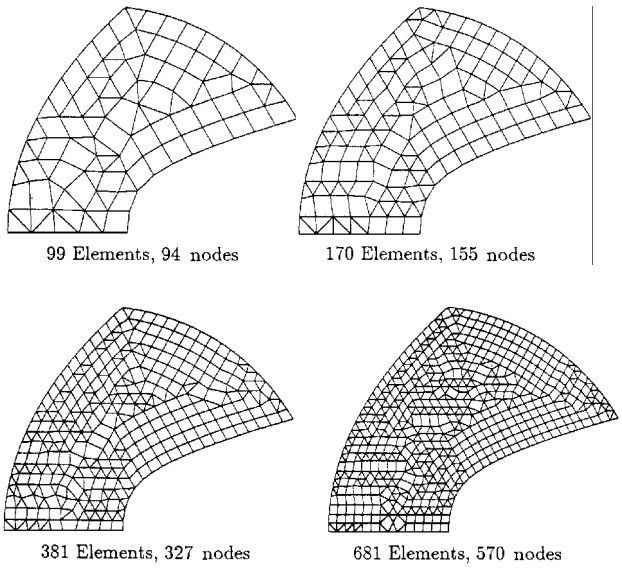


**a) Meshes**

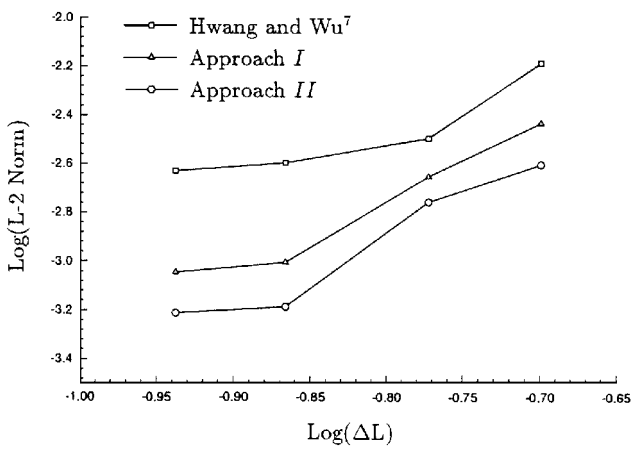


**b) $L_2$ norm of density error vs grid space**

**Fig. 2 Ringleb's flow.**

region on the lower surface of the airfoil. Also, the numerical convergence of approach II is best among the three methods. Based on the preceding discussion, approach II is preferred and will be used in the following computations.

*Shock Propagation in a Channel*

To demonstrate the ability of the present solution-adaptive approach, a shock propagation problem is studied. In this problem, the shock with a shock Mach number of 1.4 moves to the right along a $1.0 \times 0.2$ rectangular channel from the position $X = 0.0$ at $T = 0.0$. During the calculation, a coarse mesh (500 elements, 561 nodes) is used as a background grid. The coarse mesh is automatically enriched by using the original[16] and present improved solution-adaptive technique, respectively. In this case, only the density-gradient is used as the mesh-enrichment indicator. Comparing with the exact solution, the pressure distributions shown in Fig. 4 indicate that the improved solution-adaptive technique produces the highest resolution among the results.

*Traveling Vortex in a Freestream*

In this section, a traveling vortex in a low-speed freestream with a Mach number of 0.1 is tested. The flowfield schema, initial conditions, and time step for this test are the same as those of Lin and Chin.[3] In a low-speed freestream, the change in pressure at the vortex center is mainly due to the dissipation property of the numerical scheme used. The computational domain of $8.0 \times 2.0$ is uniformly divided to be a fine mesh ($333 \times 133$) or a coarse mesh ($250 \times 101$). During the calculation, the coarse mesh is used as a background grid,

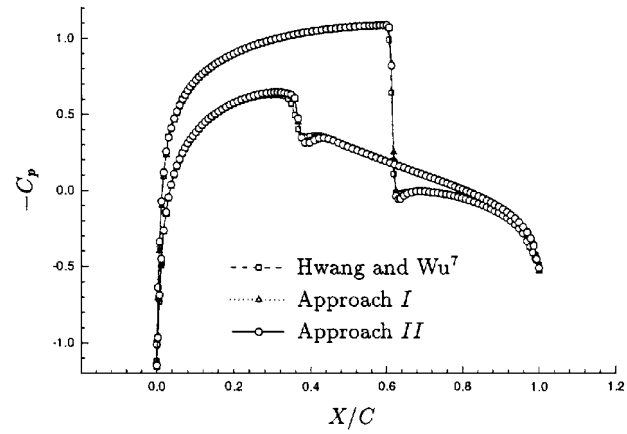


**a) Pressure coefficient distributions along the airfoil surface**

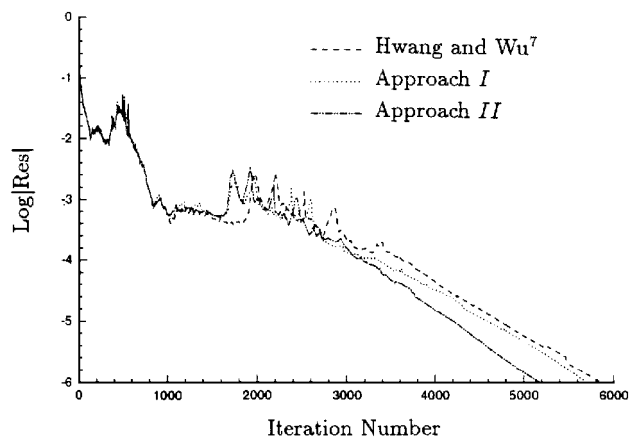


**b) Corresponding convergence histories**

**Fig. 3 Transonic flow around the NACA 0012 airfoil.**

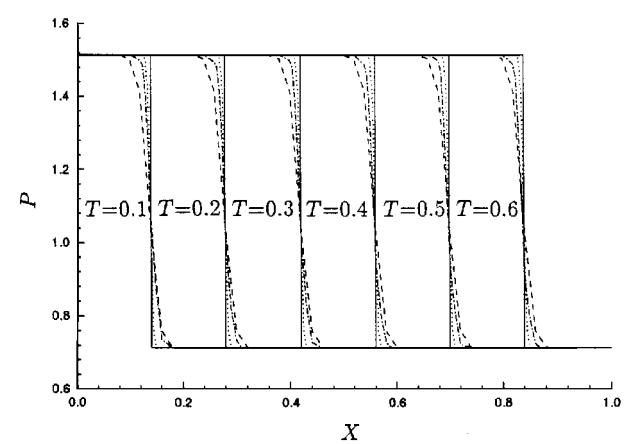


**Fig. 4 Shock propagation in a channel: The pressure distributions along the lower wall; $T$ = 0.1, 0.2, 0.3, 0.4, 0.5, and 0.6: ——, exact solution; - - - -, approach II (coarse mesh); - . - . -, approach II (solution-adaptive technique[16]); and . . . , approach II (present solution-adaptive technique).**

and it is enriched by using the present improved solution-adaptive technique. Besides the density-gradient, the vorticity is adopted as the mesh-enrichment indicator. From the variation of core pressure $P_{\text{core}}/P_{\infty}$ as a function of the length of vortex travel (see Fig. 5, vortex core radius $a_0 = 0.06$), the ability of the present scheme (approach II) to compute the advection of a vortex with minimal dissipation of the vortex strength is confirmed, and the related numerical dissipation is less than those of schemes[3,7] when fixed meshes are used. By combining with the adaptive technique, a better result than that on the fine mesh is achieved.

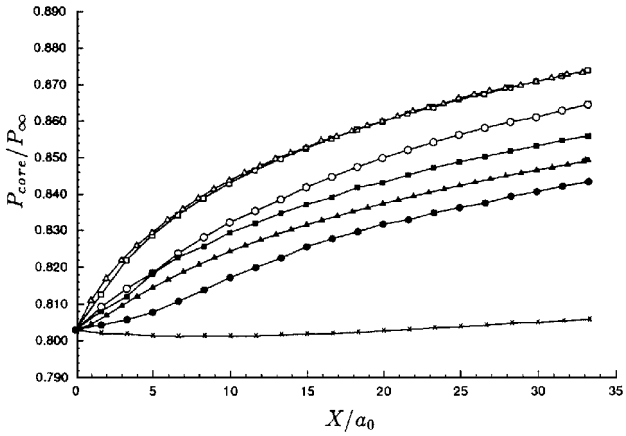


**Fig. 5 Traveling vortex in a freestream: Variation of the vortex core pressure as a function of the length of vortex travel: □, Hwang and Wu[7] (coarse mesh); △, Lin and Chin[3] (coarse mesh); ○ approach II (coarse mesh); ■, Hwang and Wu[7] (fine mesh); ▲, Lin and Chin[3] (fine mesh); ● approach II (fine mesh); and ×, approach II (adapted mesh).**

*Acoustic Pulse in a Freestream*

To examine the effectiveness of the present solution-adaptive approach for simulating the acoustic wave, an acoustic pulse in a freestream of $M_\infty = 0.5$ is tested.[18] The initial conditions and time step for this test are the same as those of Tam and Webb.[18] A pressure pulse is released at $T = 0$. Then an acoustic pulse is generated and expanded radially. Pressure pulse amplitude is $\frac{1}{100}$ of $P_\infty$ and this disturbance is relatively small so that the present Euler solutions may be compared with the exact solution of the linearized Euler equations.[18] The computational domain of $200.0 \times 200.0$ is uniformly divided into a fine mesh[18] ($201 \times 201$) or a coarse mesh ($101 \times 101$). During the calculation, the coarse mesh is used as a background grid, and it is enriched by using the dilatation mesh-enrichment indicator only. The adapted mesh at $T = 50$ is shown in Fig. 6a. Comparing with the exact solution, the pressure disturbances $(P - P_\infty)/P_\infty$ along $Y = 0$ at $T = 50$ are shown in Fig. 6b. It is evident that the adapted result is the best one among those three numerical solutions. Therefore, the present solution-adaptive upwind approach is a good candidate for aeroacoustic computations.

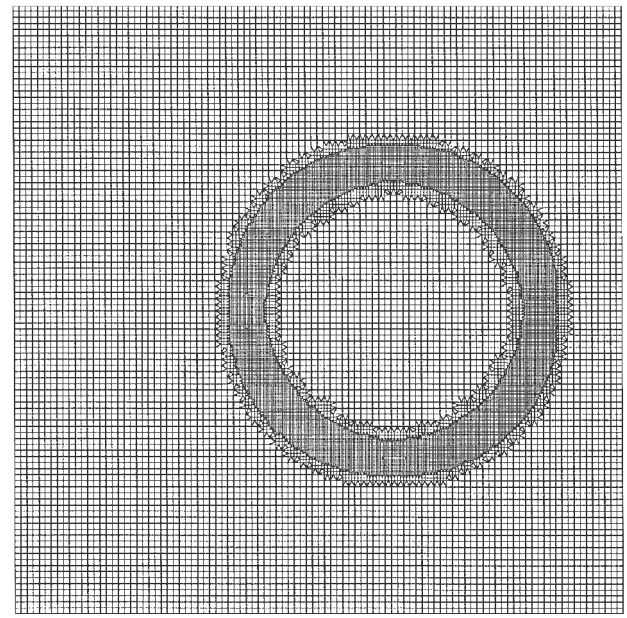

**Fig. 6a Instantaneous adapted mesh, $T = 50$.**

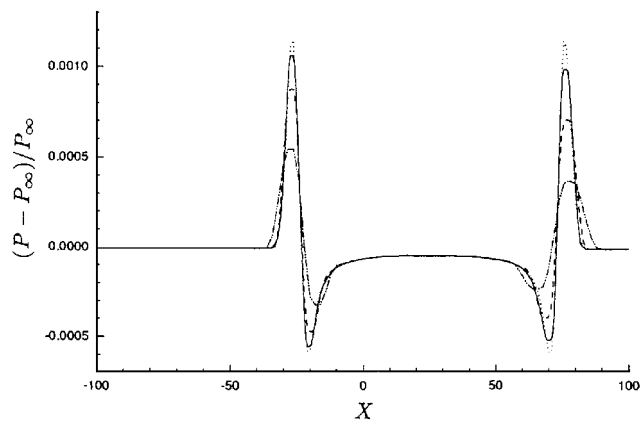


**Fig. 6b Pressure waveform along $Y = 0$; acoustic pulse in a freestream: . . . , exact solution[18]; - . - , approach II (coarse mesh); ----, approach II (fine mesh); and ——, approach II (adapted mesh).**

## Application to Aeroacoustic Computations

*VSI*

For the noise produced by rockets and high-speed aircraft, VSI is a significant source. The interaction between the vortex and shock wave and the corresponding acoustic field are studied. In the present calculations, the initial flowfield and mesh ($132 \times 122$ nodes) of the VSI problem[1] are adopted (see Fig. 7a, $T = 0.0$). First, a stationary normal shock is established approximately at the middle of a slight diverging duct by a back pressure ratio of 1.349. Then a vortex, where the mathematical expression of tangential velocity is the same as that of Ref. 1, is superimposed upstream of the shock. Figure 7a shows the instantaneous adapted meshes and corresponding pressure contours. At $T = 0.2$, the vortex is passing through the shock and twists it. On the top of the vortex center, the vortex pushes the shock wave to move downstream, and the pressure is higher than that of the initial solution (see Fig. 7a, $T = 0.0$ and 0.2). On the bottom of the vortex center, the vortex pulls the shock wave to move upstream and forces the pressure lower than the initial value (see Fig. 7a, $T = 0.0$ and 0.2). After the interaction, a cylindrical wave is expanding radially outward (see Fig. 7a, $T = 0.4$). By using the aforementioned three mesh-enrichment indicators together, the shock wave, vortex, and acoustic wave are well simulated. To verify the nature of this wave as the acoustic wave, the wavefront positions along $X = X_v$ (where $X_v$ is the $x$ coordinate of vortex core) at time $T = 0.3, 0.35, 0.4$, and 0.45 are plotted in Fig. 7b. The slope of this line represents the speed of the wavefront, and it is equal to the local speed of sound. The aforementioned phenomena were also presented by Meadows et al.[1]

*Transonic BVI*

The noise sources of helicopter rotor include discrete and broadband sources. The BVI sound is one of the important discrete sound sources. Considering a NACA 0012 airfoil at a freestream Mach number of $M_\infty = 0.76$, the initial vortex, where the velocity profile was given in Ref. 3, is released from $X_0 = -5$, $Y_0 = -0.2$ and convected downstream. The outer boundary is taken as a rectangle of $21 \times 20$ chords, and a mixed mesh (35,336 elements, 20,148 nodes) is used as the background grid. The aforementioned three mesh-enrichment indicators are used together. Figure 8a shows the instantaneous adapted meshes and corresponding pressure contours at time $T = 4.6$, 5.8, and 8.0. From the results shown in Fig. 8a, the behaviors of shock wave, vortex, and two acoustic waves are clearly observed. After the vortex passes through the shock, which is similar to the previous VSI case, the result shown in Fig. 8a ($T = 5.8$) indicates the bifurcation of shock on the lower surface of the airfoil. As indicated at $T = 5.8$ and 8.0 (see Fig. 8a), $C$ is the compressibility wave due to the displacement of stagnation point at leading edge caused by the vortex. At $T = 8.0$, $T$ is the transonic wave due to the shoulder shock wave of the airfoil emitted upstream. In Refs. 4 and 19, both aforementioned acoustic waves were also discussed. Even though the strength of the acoustic waves decreases rapidly as it goes farther away from the blade, the present solution-adaptive approach with dilatation mesh-enrichment indicator can still efficiently capture them. The variation of the vortex core pressure $P_{\text{core}}/P_\infty$ as a function of time is plotted in Fig. 8b. From

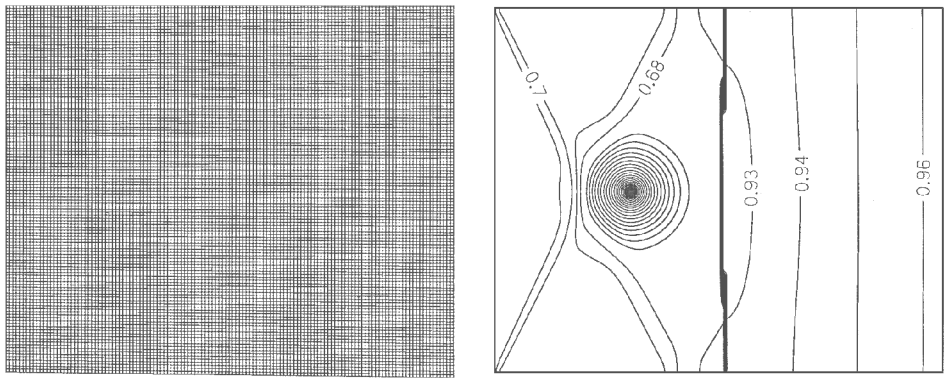


$T = 0.0$

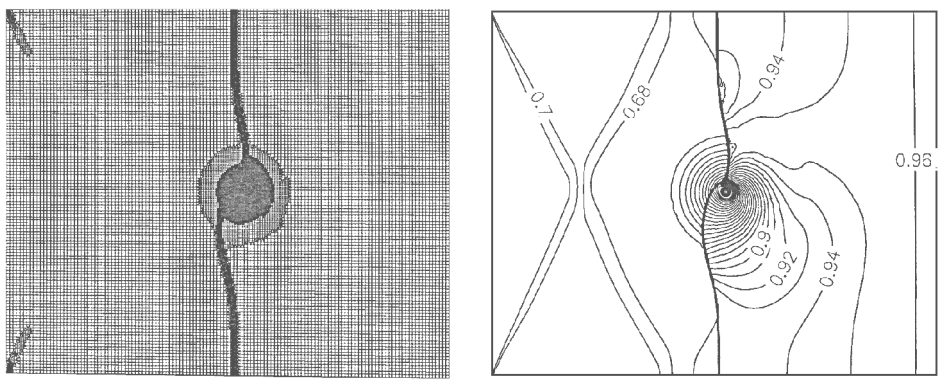


$T = 0.2$

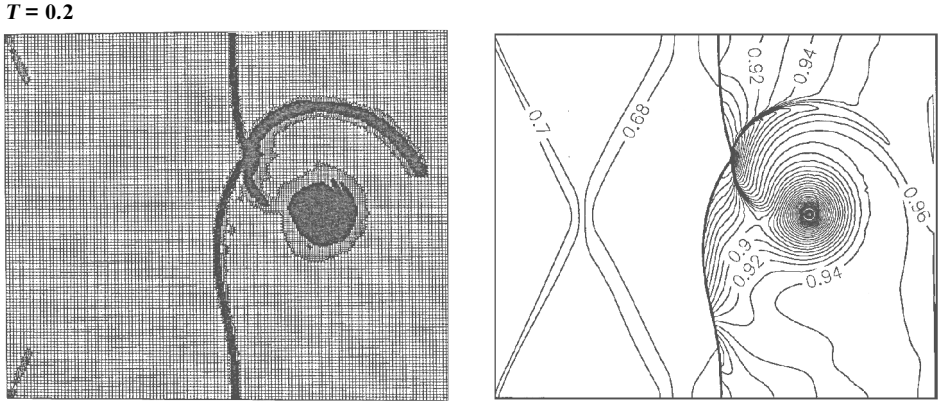


$T = 0.4$

**a) Instantaneous meshes and corresponding pressure contours**

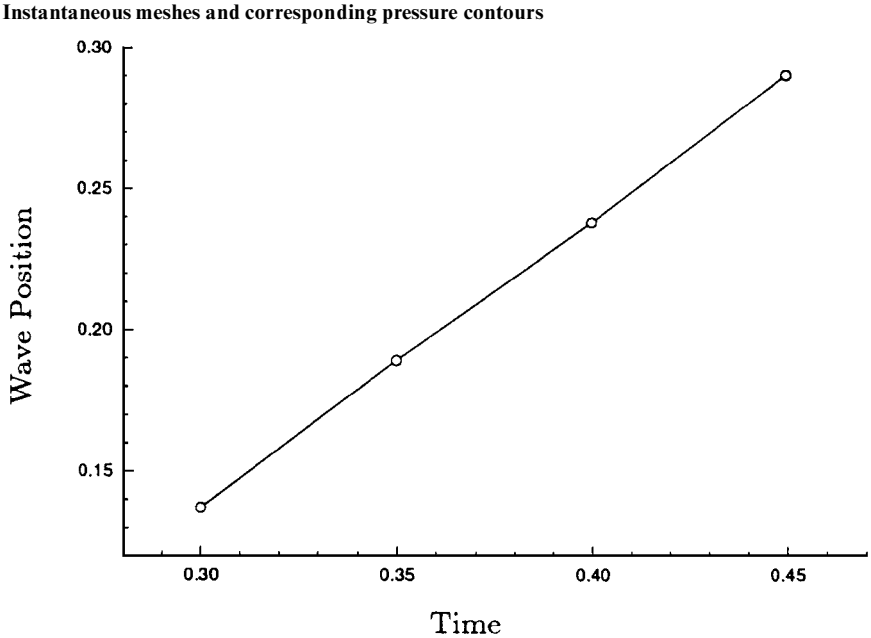


**b) Acoustic wavefront positions along $X = X_v$ as a function of time**

**Fig. 7 Vortex–shock interaction.**

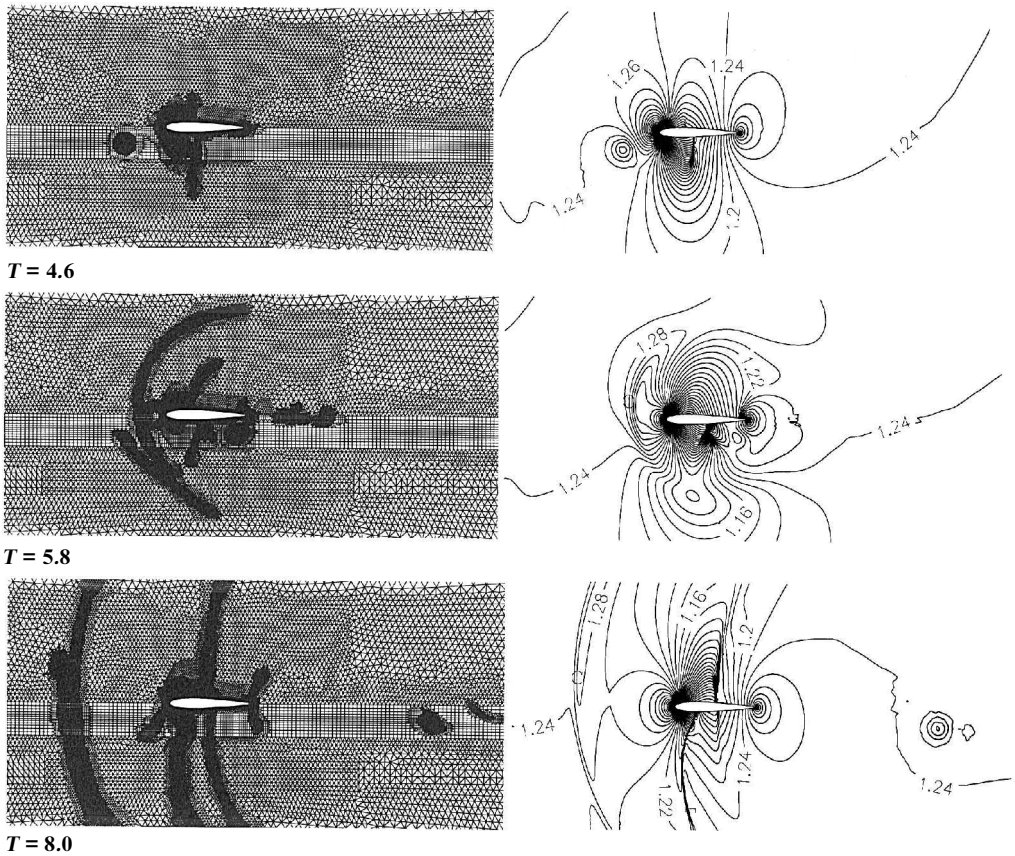


**a) Instantaneous meshes and corresponding pressure contours**

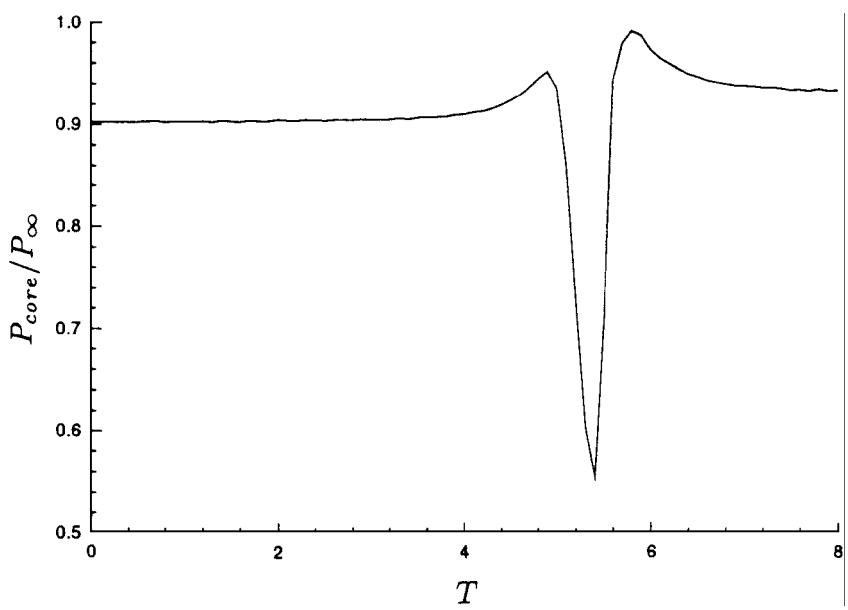


**b) Variation of the vortex core pressure as a function of time**

**Fig. 8 Transonic blade-vortex interaction.**

the preceding discussion, the present solution-adaptive approach is suitable for studying aeroacoustic problems.

## Conclusions

Solution-adaptive cell-vertex finite volume upwind approaches have been developed to solve the unsteady Euler equations on quadrilateral-triangular meshes. Those approaches include Runge–Kutta method for time integration, Roe's Riemann solver, a modified area-averaged approach, MUSCL differencing with two kinds of characteristic variables, and an improved solution-adaptive technique, where dilatation is presented as a new mesh-enrichment indicator for simulating the acoustic waves. In the computations of Ringleb's flow, the upwind approach with the second kind of characteristic variables (approach II) gives the best results. For the transonic flow around the NACA 0012 airfoil, the pressure distributions along the airfoil surface and the corresponding convergent behaviors indicate that approach II is the best one among three methods (method in Ref. 7, present approach I, and approach II). To evaluate the present solution-adaptive approach, the shock propagation in a channel, a traveling vortex in a freestream, and an acoustic pulse in a freestream are investigated. Comparing with the related exact solutions and other numerical results, it is proved that the

present approach II with improved solution-adaptive technique provides accurate and high-resolutional results. To further understand the availability of the present solution-adaptive approach for studying the complex aeroacoustic problems, VSI and transonic BVI are computed. The distorted shock wave and the cylindrical acoustic wave, which are produced by VSI, are simulated. In the BVI flowfield, two acoustic waves, transonic and compressibility waves, and shock bifurcation on the lower surface of the airfoil are predicted. Also, the variation of the vortex core pressure as a function of time is presented. Based on the results and discussion, the present solution-adaptive approach is an appropriate method for aeroacoustic computations.

## References

[1]Meadows, K. R., Kumar, A., and Hussaini, M. Y., "Computational Study on the Interaction Between a Vortex and a Shock Wave," *AIAA Journal*, Vol. 29, No. 2, 1991, pp. 174–179.

[2]Casper, J., and Meadows, K. R., "Using High-Order Accurate Essentially Nonoscillatory Schemes for Aeroacoustic Applications," *AIAA Journal*, Vol. 34, No. 2, 1996, pp. 244–250.

[3]Lin, S. Y., and Chin, Y. S., "Comparison of Higher Resolution Euler Schemes for Aeroacoustic Computations," *AIAA Journal*, Vol. 33, No. 2, 1995, pp. 237–245.

[4]Lin, S. Y., and Chin, Y. S., "Numerical Study of Transonic Blade-Vortex Interaction," *AIAA Journal*, Vol. 33, No. 8, 1995, pp. 1377–1382.

[5]Strawn, R. C., Biswas, R., and Garceau, M., "Unstructured Adaptive Mesh Computations of Rotorcraft High-Speed Impulsive Noise," *Journal of Aircraft*, Vol. 32, No. 4, 1995, pp. 754–760.

[6]Dadone, A., and Grossman, B., "Characteristic-Based, Rotated Upwind Scheme for the Euler Equations," *AIAA Journal*, Vol. 30, No. 9, 1992, pp. 2219–2226.

[7]Hwang, C. J., and Wu, S. J., "Adaptive Finite Volume Upwind Approach on Mixed Quadrilateral-Triangular Meshes," *AIAA Journal*, Vol. 31, No. 1, 1993, pp. 61–67.

[8]Whitaker, D. L., Grossman, B., and Lohner, R., "Two-Dimensional Euler Computations on a Triangular Mesh Using an Upwind, Finite-Volume Scheme," AIAA Paper 89-0470, Jan. 1989.

[9]Shu, C. W., "Total-Variation-Diminishing Time Discretizations," *SIAM Journal on Scientific and Statistical Computing*, Vol. 9, No. 6, 1988, pp. 1073–1084.

[10]Roe, P. L., "Approximate Riemann Solvers, Parameter Vectors, and Difference Schemes," *Journal of Computational Physics*, Vol. 43, Oct. 1981, pp. 357–372.

[11]Anderson, W. K., Thomas, J. L., and van Leer, B., "Comparison of Finite Volume Flux Vector Splittings for the Euler Equations," *AIAA Journal*, Vol. 24, No. 9, 1986, pp. 1453–1460.

[12]Lacor, C., and Hirsch, C., "Genuinely Upwind Algorithms for the Multidimensional Euler Equations," *AIAA Journal*, Vol. 30, No. 1, 1992, pp. 56–63.

[13]Levy, D. W., Powell, K. G., and van Leer, B., "An Implementation of a Grid-Independent Upwind Scheme for the Euler Equations," AIAA Paper 89-1931, June 1989.

[14]Powell, K. G., and van Leer, B., "A Genuinely Multi-Dimensional Upwind Cell-Vertex Scheme for the Euler Equations," AIAA Paper 89-0095, Jan. 1989.

[15]Giles, M. B., "Nonreflecting Boundary Conditions for Euler Equation Calculations," *AIAA Journal*, Vol. 28, No. 12, 1990, pp. 2050–2058.

[16]Hwang, C. J., and Fang, J. M., "Solution-Adaptive Approach for Unsteady Flow Calculations on Quadrilateral-Triangular Meshes," *AIAA Journal*, Vol. 34, No. 4, 1996, pp. 851–853.

[17]Chiocchia, G., "Exact Solutions to Transonic and Supersonic Flows," AGARD Advisory Rept. AR-211, June 1985.

[18]Tam, C. K. W., and Webb, J. C., "Dispersion-Relation-Preserving Finite Difference Schemes for Computational Acoustics," *Journal of Computational Physics*, Vol. 107, Aug. 1993, pp. 262–281.

[19]Lent, H. M., Meier, G. E. A., Muller, K. J., Obermeier, F., Schievelbusch, U., and Schurmann, O., "Mechanisms of Transonic Blade-Vortex Interaction Noise," *Journal of Aircraft*, Vol. 30, No. 1, 1993, pp. 88–93.

S. Glegg
*Associate Editor*